Cold-Sintering and Li doped ZnO Sintering Aid for the Densification of BaZr0.7Ce0.2Y0.1O3-δ Proton Conducting Ceramics

P Castellani, E Quarez, C Nicollet, O Joubert, N Gautier, P Pers, G Taillades, A Le Gal La Salle

To cite this version:

P Castellani, E Quarez, C Nicollet, O Joubert, N Gautier, et al.. Cold-Sintering and Li doped ZnO Sintering Aid for the Densification of BaZr0.7Ce0.2Y0.1O3-δ Proton Conducting Ceramics. International Journal of Hydrogen Energy, 2023, 54, pp.1343-1356. 10.1016/j.ijhydene.2023.11.228 . hal-04467636

HAL Id: hal-04467636
https://hal.science/hal-04467636

Submitted on 20 Feb 2024

Cold-Sintering and Li doped ZnO Sintering Aid for the Densification of $BaZr_{0.7}Ce_{0.2}Y_{0.1}O_{3-\delta}$ Proton Conducting Ceramics

P. Castellani[1], E. Quarez[1], C. Nicollet[1], O. Joubert[1], N. Gautier[1], P. Pers[2], G. Taillades[2] and A. Le Gal La Salle[1]

(1) Nantes Université, CNRS, Institut des Matériaux de Nantes Jean Rouxel, IMN, 2 rue de la Houssinière, F-44000 Nantes - France

(2) Institut Charles Gerhardt de Montpellier, ICGM, 1919 route de Mende, 34293 Montpellier - France

ABSTRACT

Proton conducting $BaZr_{0.9-x}Ce_xY_{0.1}O_{3-\delta}$ electrolytes have been intensively investigated in the past years. The zirconium rich stoichiometry of this perovskite type material shows good chemical stability coupled with high proton conductivity. However, this material remains highly refractory. Therefore, high sintering temperatures (1800 °C) are required to fully densify the electrolyte layer. This study focuses on using different sintering strategies, such as cold-sintering and sintering aids, during the fabrication of the electrolyte to decrease the sintering temperature. After various densification protocols, the electrical conductivity of the zirconate ($BaZr_{0.7}Ce_{0.2}Y_{0.1}O_{3-\delta}$) electrolytes are compared to study the influence of the densification process on the bulk, grain boundary and total conductivity of the electrolyte layer.

I. INTRODUCTION

Solid oxides cells have been increasingly investigated in the past decades, owing to their high faradic efficiencies [1,2]. Solid oxide cells are most commonly based on fluorite-type oxide-ion conducting materials such as yttria-stabilized zirconia. To limit ohmic losses in the cells, they typically operate at high temperature (700 - 900 °C), which causes accelerated degradation of performance [3]. More recently, new classes of ceramics were studied for their fast proton transport ability in lower temperature ranges (450 - 600 °C) [4,5]. Since the discovery of protonic conduction in strontium cerates perovskite by Iwahara and coworkers [6], many efforts concentrated on more stable perovskite materials such as barium cerate and barium zirconate [7].

Barium zirconate $BaZrO_3$ crystallizes in a perovskite structure and is already in use in the industry for its thermal refracting properties, since its melting point is around 2620 °C [8]. The material also shows excellent mechanical resistance to yield stress, high chemical and thermal stability and compatibility with a wide range of elements. Doped Barium cerate, particularly with yttrium, $Ba(Ce,Y)O_{3-\delta}$ is also a well-known material that shows high proton conductivity at intermediate temperature [9] . However, this material shows poor thermal and chemical stability, especially when exposed to carbon dioxide [10]. Therefore, solid solutions of the two perovskites were also considered, with the aim to combine the chemical stability of $BaZrO_3$ with the high proton conductivity of doped $BaCeO_3$ [11,12]. In this study, a composition with high Zr content is considered: $BaZr_{0.7}Ce_{0.2}Y_{0.1}O_{3-\delta}$ (BZCY-721) [13]. Therefore, this zirconium-rich composition shows good proton conduction and stability in presence of CO_2. Its properties make it a suitable material as an electrolyte for Proton Ceramic Fuel Cell or electrolyser (PCFC or PCEC). However, the sinterability remains the major issue of this highly refractory ceramic material. To limit processing costs and thermal stresses during sintering treatments, there is a clear incentive to reduce the temperatures required to densify those ceramics.

In the early 60s, Coble [14] proposed a detailed study explaining the different phenomenon occurring during sintering. He also stated that transparent ceramics (crystalline state of the material) could be obtained by completely removing the porosity, thus reaching the complete densification of the material. For some specific materials such as Al_2O_3, it is possible to naturally reach such relative density. However, for more refractory materials, using alternative strategies such as sintering aids is almost mandatory. For example, it is possible to use metal oxides such as ZnO, NiO, FeO, MoO_3, CuO, *etc.* as sintering aids to enhance both densification and grain growth [11,15–17]. In 2005, ZnO was first used as sintering aid for $BaZr_{0.8}Y_{0.15}O_{3-\delta}$, and the sintering temperature was reduced from 1700 °C to 1300 °C. Another study presented by Babar *et al.* [18] showed the possibility to reduce the sintering temperature to 1150 °C using a CuO sintering aid. More recently Y. Li *et al.* [19] have demonstrated that the potential of the simultaneous use of lithium and zinc oxides is effective to enhance the densification of $BaZr_{0.8}Y_{0.2}O_{3-\delta}$ (1400 °C for 8 h). Another effective way to reduce the energy consumption during sintering is to use intermediate strategies such as Cold-Sintering Process (CSP). The densification mechanisms of the CSP have been extensively studied by Guo *et al.* [20] for simple oxides. CSP uses a small amount of aqueous solution added to the ceramic powder during pressing. The solvent enables densification via a dissolution-precipitation process, while heating the material at boiling temperatures. Recently, CSP has been also applied in our group to BZCY type oxide with a high concentration of cerium, $BaZr_{0.1}Ce_{0.8}Y_{0.1}O_{3-\delta}$ [21]. The challenge here is to develop low temperature sintering for the refractory ceramic composition $BaZr_{0.7}Ce_{0.2}Y_{0.1}O_{3-\delta}$. This study compares the influence of dual sintering aids (lithium and zinc oxides) and of CSP on the densification, the morphology and the conductivity of the $BaZr_{0.7}Ce_{0.2}Y_{0.1}O_{3-\delta}$ electrolyte materials.

II. EXPERIMENTAL

Commercial $BaZr_{\mathbf{0.7}}Ce_{\mathbf{0.2}}Y_{0.1}O_{3-\delta}$ powder (Cerpotech) was used and characterized for this study. Conventional preparation of the electrolyte membrane consists in pressing the powder at 375 MPa for 10 min followed by a sintering treatment at 1600 °C for 15 h. For CSP protocol, 5 wt. % of water was added to the powder and mixed in a mortar. A simple hot-pressing dye is used to enable both heating and pressing [21]. A 375 MPa pressure is applied to the 10 mm diameter pellet and the temperature is kept at 180 °C during 1 h. The pellet is then dried overnight in an oven at 120 °C. Then, the pellet is further treated at 1600 °C during 15 h. In the protocol using sintering aids, a dual sintering aid containing 20 mol.% of lithium oxide and 80 mol.% of zinc oxide is investigated. The sintering aid powder was prepared by impregnation of a lithium nitrate solution (in ethanol) on a commercial zinc oxide powder (Aldrich). The product was dried at room temperature overnight and calcined at 700 °C for 10 h. Then, 1 wt% of the sintering aid powder is added to the BZCY-721 powder and mixed in a mortar manually. In this study, four densification strategies were used: i) the conventional sintering protocol, ii) the sintering aid protocol and iii) the CSP protocol.

The grain size distribution of the powders was measured by laser-granulometry (Masterize2000) under pressurized air and in an ultrasonic bath of absolute ethanol. Calibration of the measurement was done using the commercial powder before conducting 15 stable measurements for statistical purposes. The specific surface areas were determined by N_2 adsorption using the Brunauer, Emmett and Teller (BET) method in a Micrometrics 3flex apparatus. X-ray diffraction patterns (XRDP) of the powder and sintered commercial BZCY-721 pellet were recorded at room temperature in air using a Bruker D8 advance diffractometer in Bragg-Brentano geometry. A copper anode source of wavelength $\lambda_{Cu\ K\alpha 1} = 1.5406$ Å is used, isolated with a germanium monochromator. The data is recorded in the range 10-80° 2θ with a step size of 0.018° and 0.42 s at each step. Rietveld refinements were performed with the JANA2006 software using $Pm\overline{3}m$ and $R\overline{3}c$ space groups [22]. Crystallite size and isotropic microstrain were determined using the fundamental approach as implemented in JANA2006 [23]. Berar corrections were applied to obtain more realistic standard uncertainties [24]. The lithium doped zinc oxide sintering aid was characterized using X-ray photoelectron spectroscopy (XPS) on Surface Science Instruments using an Al K Alpha source with a spot size of 500μm. 501 energy steps were made using a step size of 0.1 eV. For each measurement ten scans were made for a total acquisition time of 4 min and 10 seconds. The spectra were analysed and fitted using the CasaXPS software. The densification behaviour of the electrolyte material was characterized by dilatometry using a NETZSCH Dil402C dilatometer, from room temperature to 1600 °C at a rate of 3 $°C\cdot min^{-1}$. The raw powder was characterized using simultaneous Thermogravimetric Analysis (TGA) and Differential Scanning Calorimetry (DSC) up to 1550 °C in dry air using a NETZSCH JUPITER 4. The morphology of the pellets and powders were characterized using Scanning Electron Microscopy (JEOL 7600 SEM). Energy Dispersive X-ray spectroscopy (EDX) was performed on polished cross sections. Samples were fractured and thermally etched at 1400 °C for 10 h. The ImageJ software was used to determine the volume density of grain boundaries after thermal etching of the cross-section. Scanning transmission electron microscopy (STEM) experiments were carried out using Themis Z G3 Cs-probe corrected microscope (Thermo Fisher Scientific) operated at 300 kV and equipped with a high-angle annular dark field (HAADF) detector, with 30mrad convergence angle. Elemental maps were acquired in STEM mode using a Super-X emission X-ray spectrometer consisting of four windowless silicon-drift detectors (SDDs) providing a large collection solid angle of 0.7 rad. In order to limit electron beam damages the samples were cooled at 96K.

The relative density of the sample before and after densification is obtained using the ratio between measured and theoretical density. The theoretical density is calculated using the equation 1.

$$\rho_{th} = \frac{Z * M}{N_a * V} \tag{1}$$

where Z is the coordination number of the cubic lattice, M the molar mass of the material, N_a the Avogadro constant and V the theoretical lattice volume of the material. The measured density is determined geometrically by measured the mass and volume of the pellets. The relative density is the ratio between measured density and theoretical density.

For electrochemical measurements, symmetrical cells were prepared [25]. One ink of $Ba_{0.5}Sr_{0.5}Co_{0.8}Fe_{0.2}O_{3-\delta}$ (BSCF) and a second one of a composite $BaZr_{0.7}Ce_{0.2}Y_{0.1}O_{3-\delta}$ / $Ba_{0.5}Sr_{0.5}Co_{0.8}Fe_{0.2}O_{3-\delta}$ (50/50 wt%) were prepared. The inks were prepared by mixing the oxide powder and ethyl-cellulose (as binder) in α-terpineol. The inks were further mixed in a three-roll mill for better homogeneity. A multi-layer electrode was deposited by screen-printing. The first layer was the composite material deposited as an interface layer to enhance the mechanical resistance of the electrode and reduce the resistive contribution of the interface to the conductivity. The second layer was made of pure BSCF. After optimization of current collection considering several current collection materials ($La_{0.6}Sr_{0.4}Co_{0.2}Fe_{0.8}O_{3-\delta}$, $La_{0.5}Sr_{0.5}MnO_3$, Silver and Platinum), and Pt was selected. Finally, the three layers were sintered at 1100 °C for 1 h.

Impedance diagrams were recorded using the Bio-logic SAS model VSP-300 potentiometer. Measurements were taken every 50 °C while decreasing the temperature from 750 °C to 100 °C. Measurements were repeated in dry and wet (3 %) synthetic air (N_2 and O_2, Alphagaz^{TM} 2 grade, Air Liquide). Validity of the measurements were controlled using the built-in Kramer-König test from the EC-LAB software (Biologic SAS). Frequency sweeps were performed from 1 MHz to 100 mHz using an amplitude of 100 mV, chosen after optimizing the signal to noise ratio while addressing the linearity requirements. In order to quantify the electrolyte contributions, the impedance diagrams of the symmetrical cells were fitted [26] with appropriate equivalent circuits using the ZVIEW software (Scribner Associates).

III. Results and discussion

The electrolyte material conductivity depends on the grain growth and densification *i.e.* high relative density yields high conductivity. The study compares the impact of several sintering strategies on the morphology and electrochemical properties of the electrolyte material.

III.1 Structural analysis of the electrolyte

$BaZr_{0.7}Ce_{0.2}Y_{0.1}O_{3-\delta}$ crystallizes in a perovskite-type structure. The XRDP recorded at room temperature of the powder as received and of the sintered pellet were refined in the possible space groups $Pm\overline{3}m$ and $R\overline{3}c$ [27]. The XRDP of the powder as received shows small impurity peaks corresponding to $BaCO_3$ (Figure 1a) while the XRDP of the sintered pellet shows a pure perovskite phase (Figure 1b). The presence of $BaCO_3$ suggests that the commercial powder is slightly deficient in barium which would explain the slightly smaller volume than that of the sintered pellet. Indeed, in the latter, barium from $BaCO_3$ can be dissolved in the perovskite lattice, thus increasing its volume.

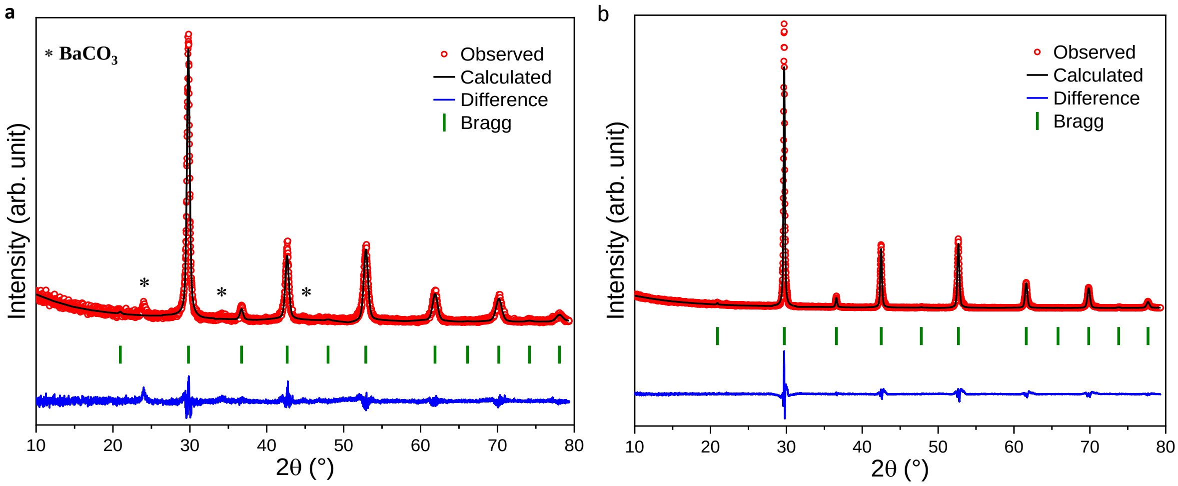

Figure 1 - X-ray diffraction patterns, and Rietveld refinements in the $Pm\overline{3}m$ *space group of commercial BZCY721 powder (a) as received, and (b) after sintering at 1600 °C for 15 h*

The results of the Rietveld refinement are reported in Table 1. The refinements in the $Pm\overline{3}m$ and $R\overline{3}c$ space groups give almost identical results with respect to R-factors, microstructural parameters, and isotropic displacement parameters. However, the $Pm\overline{3}m$ space group gives slightly better R_{Bragg} than in the $R\overline{3}c$ space group. This result, coupled with the lack of visible superstructure peaks in the patterns, leads to consider refinements in the $Pm\overline{3}m$ space group. Figure 1 shows the final plots of the Rietveld refinements in the $Pm\overline{3}m$ space group. As expected from the temperature increase, the crystallite size of the sintered pellet (103 nm) is larger than that of the commercial powder (36 nm). The line broadening of the diffraction peaks is also affected by microstrain which is due to multiple substitutions in the same 1*a* site of the cubic structure. The microstrain decreases significantly, from 0.2 to 0.04%, after sintering.

Table 1. *Structural parameters obtained from Rietveld refinement of the powder and sintered pellet of commercial BZCY721. For refinements, the Ba site occupancy is set to full, the Zr, Ce and Y occupancies are set to 0.7, 0.2 and 0.1, respectively and the O site occupancy is set to obtain the formula* $BaZr_{0.7}Ce_{0.2}Y_{0.1}O_{2.95}$. $^{a}V_c$ *is*

the volume per unit formula. [b]For the x-coordinate of oxygen in the $R\bar{3}c$ space group, the value was set to 0.5 due to instability.

	As received		Sintered (1600°C)	
Space group (no.)	$Pm\bar{3}m$ (221)	$R\bar{3}c$ (167)	$Pm\bar{3}m$ (221)	$R\bar{3}c$ (167)
a (Å)	4.2371(8)	5.988(7)	4.2536(2)	6.0125(7)
c (Å)		14.70(4)		14.750(3)
V (Å^3), V_c (Å^3)[a]	76.07(3)	456.4(14), 76.07	76.959(8)	461.76(13), 76.96
Z	1	6	1	6
χ^2	1.23	1.23	1.32	1.32
R_p (%)	12.92	12.93	15.29	15.30
R_{wp} (%)	19.09	19.09	21.50	21.48
R_{Bragg} (%)	2.13	2.30	2.23	2.43
Microstructural parameters				
Crystallite size (nm)	36(2)	36(2)	103(4)	104(4)
Microstrain ε_0 (%)	0.198(7)	0.195(11)	0.042(3)	0.035(4)
Isotropic displacement parameter U_{iso} (Å^2), Wyckoff position and x-coordinate for O in the $R\bar{3}c$ space group				
U_{Ba} in 1b	0.017(4)	-	0.012(3)	-
$U_{Zr/Ce/Y}$ in 1a	0.002(4)	-	0.002(3)	-
U_O in 3d	0.010(9)	-	0.013(9)	-
U_{Ba} in 6a	-	0.017(4)	-	0.012(3)
$U_{Zr/Ce/Y}$ in 6b	-	0.002(4)	-	0.002(3)
U_O in 18e, x	-	0.010(9), 0.5[b]	-	0.008(10), 0.478(10)

III.2 Specific surface area and grain size distribution of the powder

As powder morphology is critical for describing sintering behavior, the specific surface area and grain size distribution of the commercial electrolyte were studied. Figure 2 shows the particle size distribution measured by laser granulometry. The presence of agglomerates in the powder results in a bimodal distribution. The median repartion d50 of the particles can be separated in two sections at the inflection point. Particles of the first section are measured between 800 nm and 2 µm and represent 28 % of the particle volume density. Particles size of the second section are measured between 5 and 11 µm and represent 25 % of the particle volume density . The particle size measured by granulometry is higher than the cristallite size calculted using Rietveld refinement. This difference can be explained by the presence of agglomerates in the powder during the granulometry measurments [28].

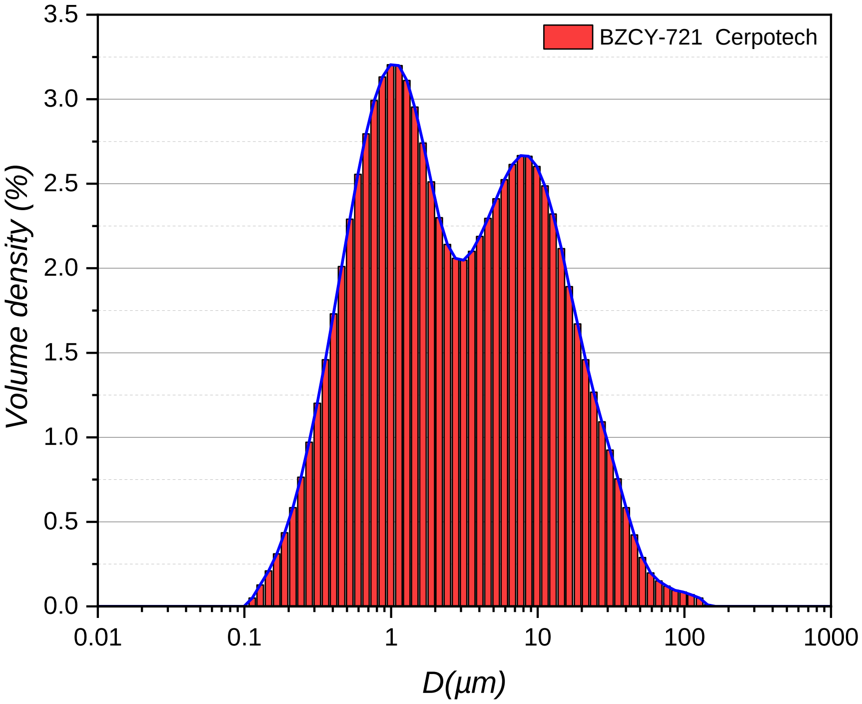

Figure 2 - Grain size distribution of the Cerpotech commercial powder measured by laser granulometry

BET measurements shows that the powder specific surface area decreases from 20 to 0.08 $m^2 \cdot g^{-1}$ after heat treatment at 1600 °C for 15 h. This behavior is consistent with grain coarsening during the densification process. However, the sensitivity of N_2 adsorption might be to low for sintered grains, which limits the precision of the measurement, even with a large amount of powder.

III.3 Characterization of the dual sintering aid

The phase composition of the pure lithium doped (20 wt%) ZnO powder was studied by X-ray diffraction. Figure 3 shows the XRD patterns of ZnO and Li doped ZnO samples. The positions of the Bragg peaks match well with the reported XRD pattern of the Wurtzite structure of ZnO (JCPDS: 89–1397). No additional phases with zinc and/or lithium compound were detected from the XRD patterns. However, small shifts in the position of the diffraction peaks towards higher angles are observed and indicate a contraction of the unit cell, consistent with Li substitution for Zn in the ZnO lattice. Indeed, Li^{1+} has a smaller ionic radius (0.60 Å) in comparison to Zn^{2+} (0.74 Å) ion. It was found that the hexagonal lattice parameters (a = 3.24 Å and c = 5.21 Å) are close to those reported in the literature [29].

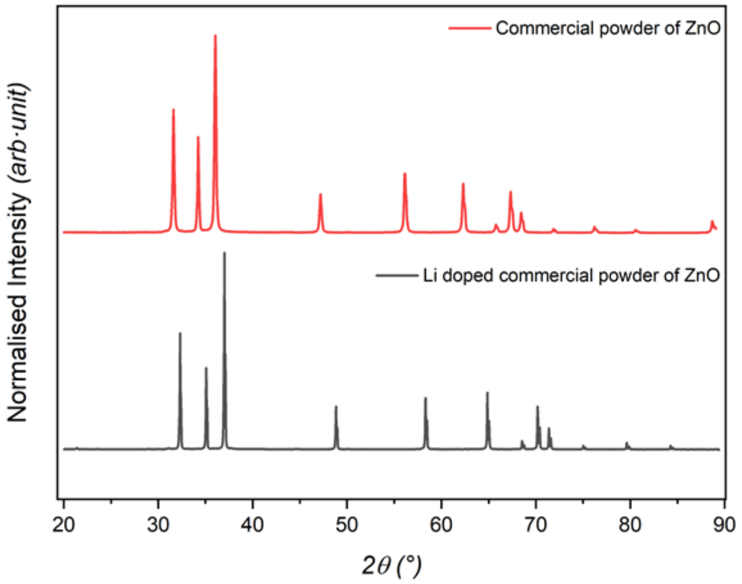

Figure 3 - X-ray diffraction patterns of commercial Zinc oxide powder and the Lithium doped Zinc Oxide powder

Additionally, the oxidation states of lithium and zinc were studied by XPS. The binding energy level of Carbon C 1s (285 eV) was used as a reference energy level and all XPS spectra were shifted according to C 1s energy level. In Figure 4a it is possible to see that the carbon peak is influenced by two chemical compositions. The C-C reference at 285 eV and the presence of carbonates (CO_3) at 290 eV. Figure 4 shows the full-scale measurement of the 20 mol% Li doped ZnO sample (figure 4a), Zn 2p (figure 4b) and Li 1s (figure 4c) binding energy were analyzed. The Zn 2p and Li 1s peaks were fitted using the CasaXPS software and all the fitting parameters are referenced in Table 2. In the Zn 2p region, the XPS spectra shows two peaks located at 1021.5 eV and 1044.9 eV corresponding to the Zn $2p_{3/2}$ and Zn $2p_{1/2}$ states. The spin–orbit splitting of 24 eV for Zn-$2p_{3/2}$ and Zn-$2p_{1/2}$ confirms that the Zn atoms are in a completely oxidized state in the sample. Li 1s signal appearing at a binding energy of 55.1 eV also shows two chemical contributions. The first contribution corresponds to Li_2O (66.58 %) fitted at 54.98 eV. The second contribution corresponds to $LiCO_3$ (33.42 %) and is fitted at 55.88 eV, its presence being supported by the carbonate contribution to the C 1s peak. In this study, no binding energy positions due to metallic lithium cluster (52.3 eV) and interstitial Li atoms (52.9 eV) [30] was detected by XPS. Therefore, the XPS results confirm that 66.58 % of lithium substitutes well the Zinc atoms.

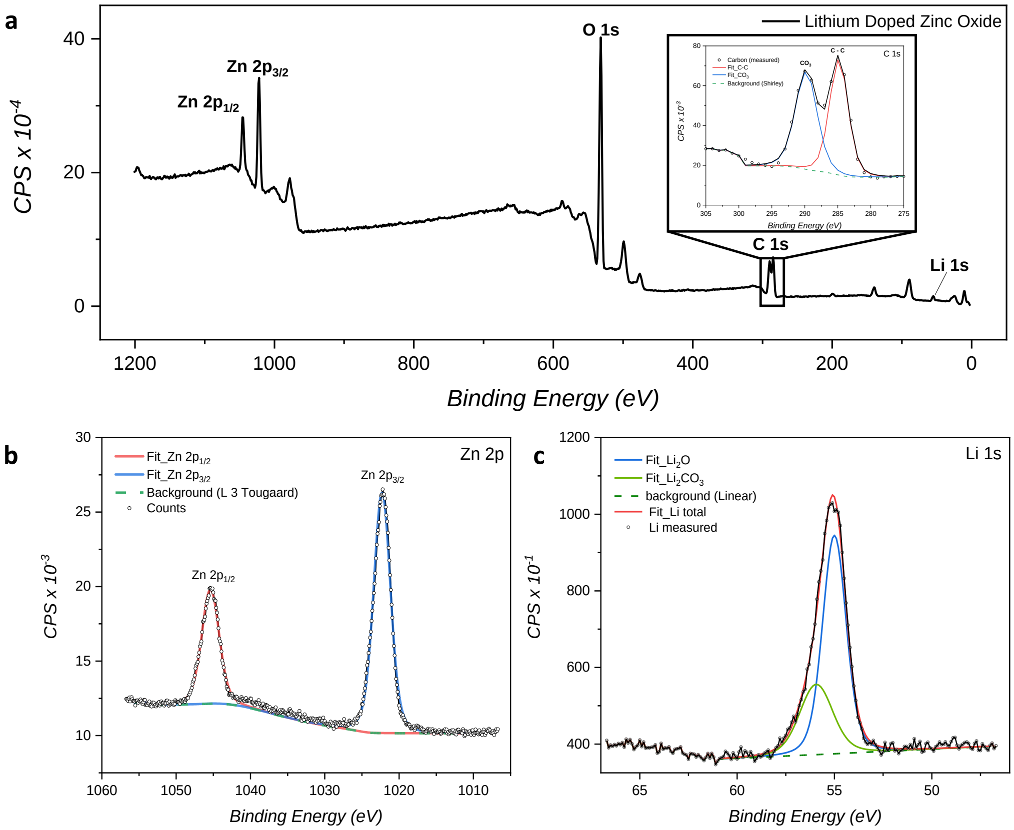

Figure 4 - (a) X-Ray photoelectron spectrometry measurements of Li doped ZnO, (b) Scan for Zn 2p and (c) Li 1s binding energy levels

Table 2. *XPS measurement fitting parameters used in Figure 4b and 4c*

	Li 1s		Zn 2p	
	Li_2O	Li_2CO_3	1/2	3/2
Fwhm	1.36703	1.81595	2.60566	2.69236
Area	876.9	440.2	48116.1	23458.1
Position	54.98	55.88	1022.28	1045.38
Line Shape	LA(1.3.230)	LA(1.3.230)	LA(1.3.230)	LA(1.3.230)

%Concentr.	66.58	33.42	67.23	32.77

III.4 Conventional sintering, cold sintering and sintering aids processes

The presence of open pores inside the electrolyte layer compromises the gas tightness of the electrolyte, leading to cross diffusion of gases from the fuel and air compartment of the cell. Therefore, it is mandatory to reduce the porosity of the electrolyte by enhancing the densification during sintering. In this section, the morphology of pellets is compared and discussed with respect to the densification protocol. Three cases are considered: pellets prepared with conventional sintering, CSP and sintering aids. To investigate the impact of the different sintering protocols on the grain growth and the grain boundary density, thermal etching [9,31,32] was performed on cross sections of the samples to reveal the grain boundaries. SEM images of the cross sections of samples prepared with the three protocols are shown in Figure 5. Grain size and concentration calculated using ImageJ software are applied to the SEM images (Table 3). For conventional sintering (Figure 5a), the high number of grains and their small size shows a limited grain growth. Figure 5b shows SEM images of sample fabricated using CSP. The cross section shows a grain morphology characterized by the heterogeneity of the grain shape and size. However, the grain number is lower than that of the conventional sintering sample, suggesting that CSP facilitates grain coarsening. In contrast, using sintering aid (Figure 5c) gives the highest relative density value, with low porosity and large grain, suggesting that the sintering aids increases grain coarsening.

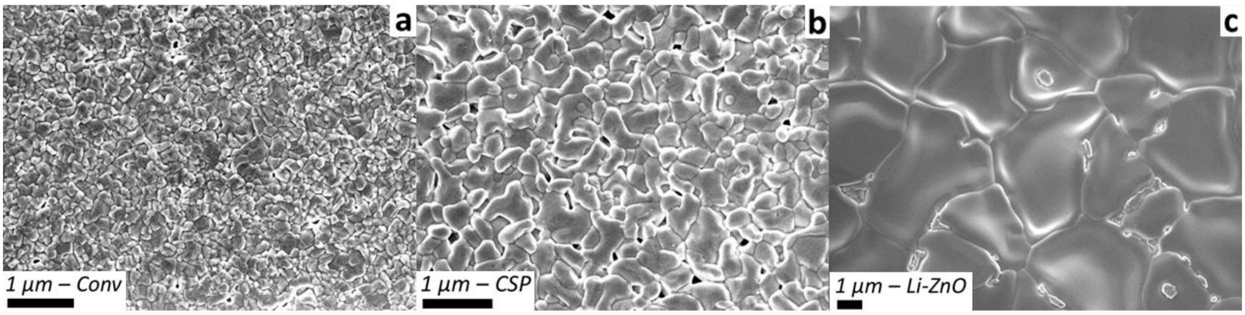

Figure 5 *- SEM images of* $BaZr_{0.7}Ce_{0.2}Y_{0.1}O_{3-\delta}$ *pellets cross sections, densified by (a) conventional sintering, (b) ZnO-Li 1wt% sintering aid (c) CSP at 180 °C before sintering*

Table 3. *Grain density values calculated with ImageJ from SEM cross section images after thermal etching*

Sintering protocol	Conventional	CSP	ZnO-Li
Grain count (grain)	50	86	26
Count Area (µm²)	4.52	26.1	409
Mean grain diameter (µm)	0.35	0.55	3.3
Grain Density (grain.µm^{-2})	11	3.3	0.06

As shown in table 3, conventional sintering yields low grain coarsening, exemplified by a high grain density (11 grain·µm^{-2}). The presence of lithium doped zinc oxide increases grain coarsening dramatically, yielding a grain density one order of magnitude lower than that of the conventional sintering (0.2 grain·µm^{-2}). The CSP yields a grain density of 3.3 grain·µm^{-2}.

Then, the crystalline structure of the densified samples is studied by X-ray diffraction (Figure 6). For samples densified conventionally and with a sintering aid, the material structure is single-phase with narrow diffraction peaks. For the CSP strategy, the X-ray diagram shows that each diffraction peak has a shoulder systematically to its right, indicating the presence of two phases: a majority phase corresponding to the main peaks, and a minority phase corresponding to the shoulders, whose composition is close to that of the majority phase and whose lattice parameter is slightly lower than that of the majority phase. The addition of water to the powder could influence the structure *via* the formation of hydroxides during the hot-pressing stage, which, being complex to decompose, would slow the crystallization of the structure, and prevent the formation of a single-phase material.

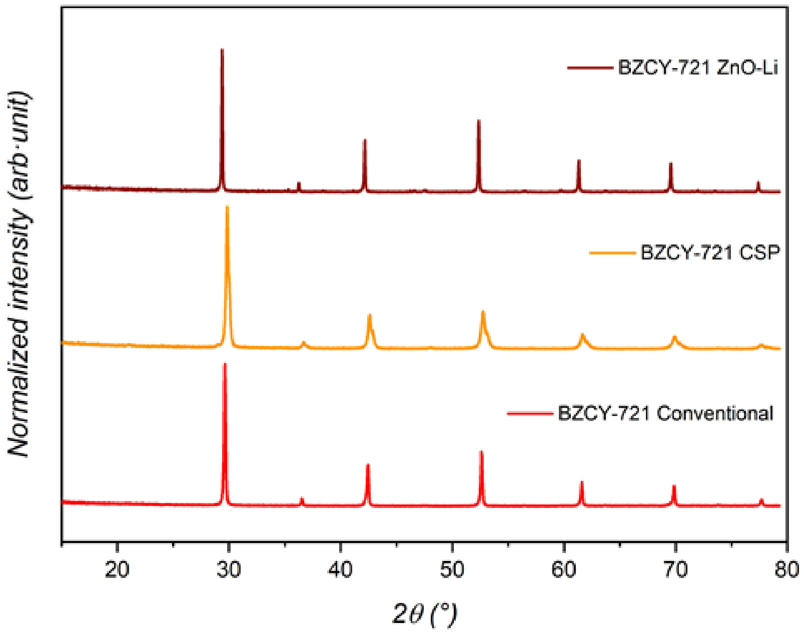

Figure 6 – XRD diagrams of the BZCY-721 samples densified following the three strategies.

Because there are two morphology properties affected by the processing protocol, namely densification and grain growth, dilatometry measurements were performed to further characterized the densification mechanisms. Figure 7a shows the sintering curves measured by dilatometry. Green pellets for conventional sintering (a), and sintering aid (b) protocols shows similar initial relative densities around 42 %. For the pellet prepared by conventional sintering, densification begins around 1000 °C before reaching a disruption at 1400 °C. This disruption is overcome around 1500 °C, after what the pellet density increases again, to reach a relative density of 66 % at 1600 °C. For the sample fabricated using sintering aid (b), densification also starts around 1000 °C. However, the disruption occurs at temperatures lower than for the conventional sintering, beginning at 1100 °C, and ending at 1400 °C. This disruption is more pronounced than that of the conventional sintering. Finally, the relative density reaches 96 % at 1600 °C. Here, the sintering mechanism is linked to the reactivity of ZnO-Li with the Barium oxide present at the surface of the grains. The sintering aid reacts to form a mixed Barium-Zinc oxide phase at the grain boundary [9]. By tuning the chemistry of the grain surface, the melting temperature of the grain boundary is decreased, owing to the formation of an eutectic (1099 °C) [33]. Moreover, the addition of lithium oxide decreases the formation temperature of the eutectic [34], thus increasing the diffusion kinetics. The cation diffusion in the liquid phase being high as compared to solid state diffusion, sintering aids leads to grain coarsening and growth. After densification, high concentration of ZnO are usually measured inside the grain boundary, whereas low concentrations are measured inside the bulk [35]. For the sample including CSP in its fabrication protocol (c), the relative density of the green pellet is higher, around 50 %. Similarly, to the conventional sample, the sintering process of the CSP sample begins around 1000 °C and yields a final relative density of 79 % at 1600 °C. The disruption is still observable at 1450 °C, but at a smaller magnitude.

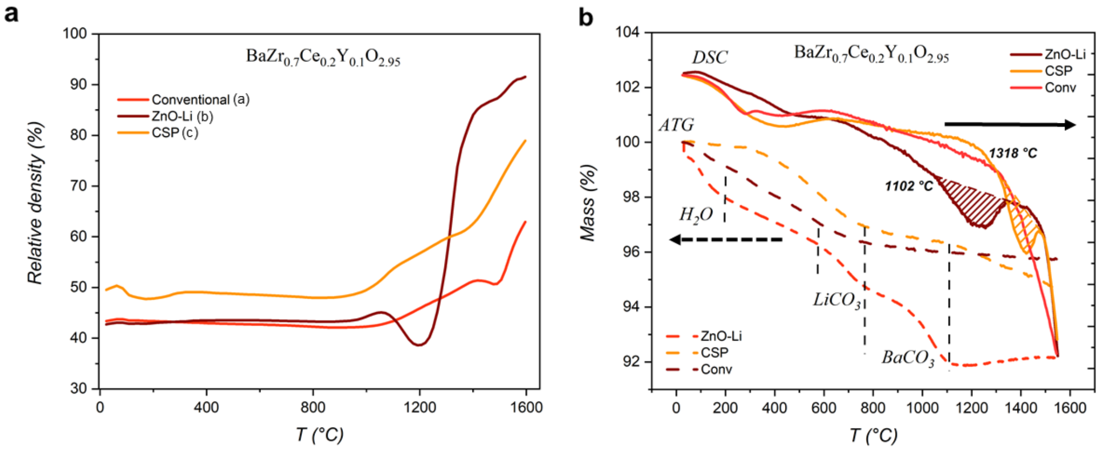

*Figure 7 - Temperature dependence (up to 1600 °C) of the relative density and geometrical shrinkage of the of $BaZr_{0.7}Ce_{0.2}Y_{0.1}O_{3-\delta}$ pellets measured by **(a)** dilatometry based on the different sintering strategies, (a) conventional sintering, (b) ZnO-Li 1 wt% sintering aid and (c) CSP. Evolution of the $BaZr_{0.7}Ce_{0.2}Y_{0.1}O_{3-\delta}$ pellet, **(b)** characterized using TGA and DSC (up to 1550 °C), fabricated using the different sintering strategies*

These results confirm that the various sintering strategies have a significant impact on the densification mechanisms. The energy loss linked to the observed disruption could be associated to the decomposition of the Barium carbonate impurity. The reaction produces carbon dioxide, which is released in the furnace atmosphere and barium oxide. Moreover, barium oxide is incorporated inside the structure [36,37]. It is also shown that using sintering aids decreases the activation energy of the decomposition reaction and facilitates the re-incorporation of barium oxide thus improving the densification.

The decomposition of the barium carbonate and the barium oxide incorporation phenomenon, inside the various electrolyte pellets, is studied in Figure 7b, showing TGA/DSC measurements conducted in similar conditions to dilatometry, coupled to a mass spectrometer. During the measurements the mass spectrometer only identified the presence of molecular weight between 43 and 45u which corresponds to the emission of CO_2. The mass spectrometer does not detect lithium or barium, which confirm that there is no cation evaporation during sintering. For the conventional sample (red), TGA measurements shows 4 % mass loss below 800 °C, related to evaporation of the residual humidity. DSC shows that the onset of the exothermic phenomenon occurs around 1400 °C, which can be correlated to the disruption observed by dilatometry. The refractive behaviour of this sample implies that the temperature is not high enough to reach the energetic feature observable on the other samples. It also means that the decomposition of the barium carbonate is not complete. The absence of the impurity decomposition could explain the very low relative density of the sample after dilatometry measurements. The CSP sample (yellow) is also marked by a loss of 3 % mass under 1000 °C. The absence of the evaporation step can be linked to the drying step of the CSP pellet after the hot pressing. The DSC show the disruption in between two exothermic steps, the first one around with an onset 1318 °C could indicates the carbonate decomposition followed by diffusion of barium and grain coarsening over 1500 °C. The pellet densified with sintering aids (wine) loses 3 % of mass between room temperature and 400 °C, linked to the evaporation of residual humidity. Between 400 and 800 °C, the pellet loses an additional 2.5 % mass, that could be explained by the decomposition of the lithium carbonate occurring after 690 °C [38]. The remaining 2.5 % mass loss corresponds to the barium carbonate decomposition between 800 and 1300 °C. Moreover, an energetic feature similar to the CSP sample can be observed, where the exothermic response has an onset around 1102 °C follow by a transition marked by an endothermic phenomenon before beginning the densification process. The reaction enthalpy for the decomposition of barium carbonate is measured around 227 $kJ.mol^{-1}$, comparable to the 230 $kJ.mol^{-1}$ found in the literature [39]. Since the carbonates were decomposed, the barium in excess needs to be reincorporated into the structure of the material. As the decomposition of the barium carbonate impacts the mass and thermal response of the electrolyte material, it could interfere with the densification process, thus slowing it down. Figure 7 supports well this hypothesis, mainly for the sintering aided and CSP samples where the sintering process begins only after complete decomposition of the Barium carbonate impurity. This delay of the sintering comes in addition of the natural refractive behaviour of the electrolyte material and is exemplified for the conventional pellet where the measured temperature range is not wide enough to observe the complete phenomenon.

III.5 Bulk and grain boundary conductivity

In order to complete the densification and reach relative densities superior to 90 % the electrolytes were sintered at 1600 °C for 15 h. In dense ceramics, conductivity depends on intrinsic factors such as charge concentration and mobility in the crystal lattice, and on extrinsic factors such as diffusion across grain boundaries [31,40]. In proton conducting ceramics, it has been shown that proton transport across grain boundaries can be orders of magnitude slower than that of the bulk, and limit the total conductivity [41]. Because the various protocols studied here, yields dramatically different microstructures, their conductivity are measured by impedance spectroscopy and compared.

Figure 8 shows, as an example, the Nyquist diagrams of the Pt//BSCF//BCZY-BSCF//BCZY symmetrical cell, measured at 200 °C and 500 °C in humidified air (p_{H_2O} = 0.02 atm). The diagrams show a series of depressed semi-circles that can be fitted by an appropriate equivalent circuit displayed above each of them. The impedance of the CPE element is given by equation (2).

$$\boldsymbol{Z_{CPE} = \frac{1}{Q_{CPE}(jw)^p}} \qquad \textbf{(2)}$$

where $\boldsymbol{Q}_{CPE}$ is the pseudo capacitance and $\boldsymbol{p}$ is the depression angle parameter. The equivalent capacitance, in F cm^{-2}, is calculated using the equation (3) [26,31,40].

$$\boldsymbol{C_{eq} = \frac{(R_{meas} \cdot Q_{CPE})^{\frac{1}{p}}}{R_{meas}}} \qquad \textbf{(3)}$$

where C_{eq} is the equivalent capacitance, and R_{meas} the measured resistance of the R-CPE parallel circuit. The Nyquist plot displayed in Figure 8a is composed of three different semi-circles, where $C_0 = 10^{-11}$ F.cm^{-2} and $C_1 = 10^{-9}$ F.cm^{-2} correspond to the bulk and grain boundary contribution, respectively. The presence of a $C_2 = 10^{-7}$ F.cm^{-2} shows the evolving electrode contribution and the beginning of the charge transfer phenomenon. As the temperature increases, all contributions are shifted to higher frequencies and it becomes impossible to discriminate the bulk and grain boundary contributions. Therefore, in Figure 8b, $R_{electrolyte}$ corresponds to bulk and grain boundary contributions. Moreover, C_2 and C_3, of respective capacitance of 10^{-7} and 10^{-5} F.cm^{-2} correspond to the charge transfer and adsorption/dissociation reaction of oxygen and water occurring inside the electrodes. The conductivity of the electrolytes prepared by the different sintering routes was derived from impedance diagrams by determining R_0 and R_1 values, which are not affected by the electrode contribution. After fitting of the impedance data to obtain the resistive contribution of each phenomenon, the conductivities of the samples were calculated by taking into account the geometry of the samples.

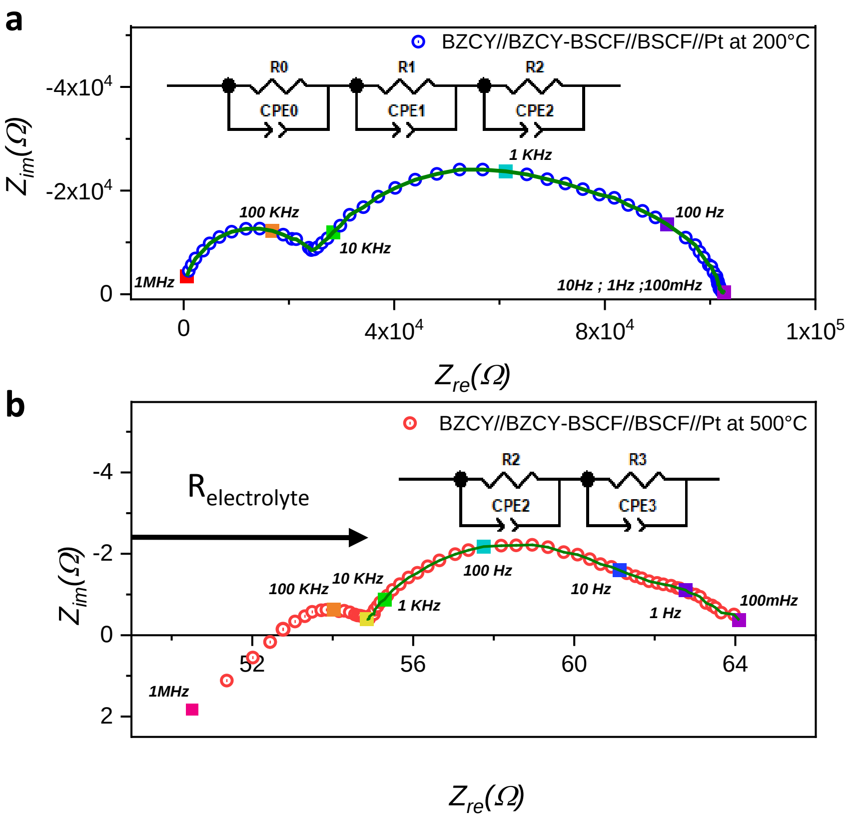

Figure 8 - Nyquist plot of the Pt//BCZY-BSCF//BCZY//BCZY-BSCF//Pt symmetrical cell at 200 °C (a) and 500 °C (b) under humid air and corresponding equivalent circuit. BCZY sample has been sintered at 1600 °C for 15 h

Figure 9 shows the temperature dependence on the bulk and grain boundary conductivities of the different sintering processes, on an Arrhenius plot. The grain interior and grain boundary (a,b) have been characterized at low temperatures in wet (3%) synthetic-air between 350 and 100 °C. The bulk conductivity (Figure 9a) is similar for all sintering processes, which confirm that it is primarily intrinsic, *i.e.* not affected by microstructure. The activation energy for the bulk conductivity is around $E_A = 0.5 \pm 0.2$ eV for all processing routes, which is consistent with proton transport in perovskite type compounds [41]. Figure 9b shows the temperature dependence of the grain boundary conductivity, which is clearly affected by the various sintering strategies. Compared to the conventional sintering route, the use of sintering aids seems to improve the grain boundary conductivity, while the CSP route yields lower grain boundary conductivity. The contribution of the grain boundary transport is influenced by both the chemistry of the grain boundary (segregation of charged defects, space charge, crystallinity), and by their concentration. Indeed, more grain boundaries will yield higher resistance.

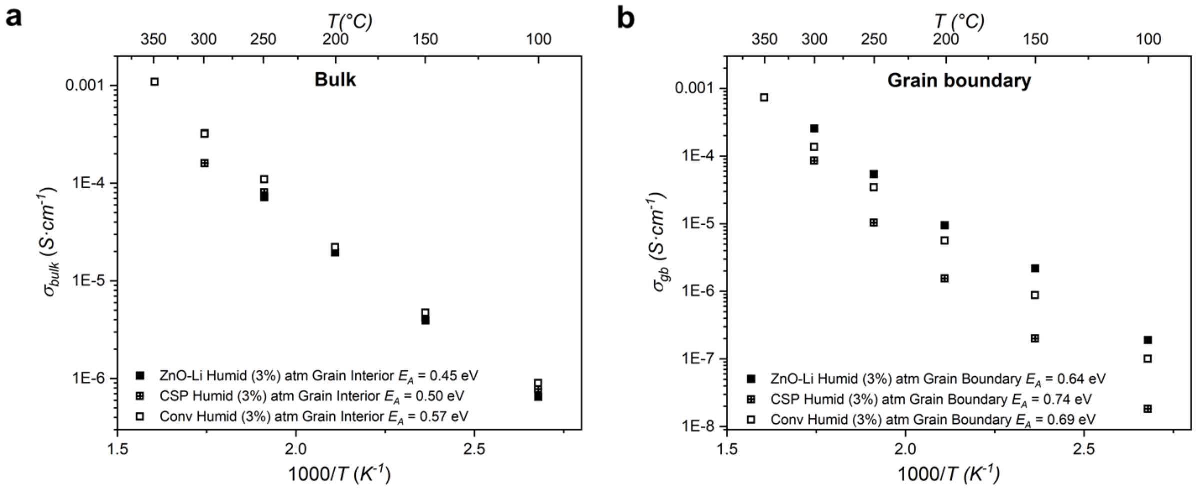

Figure 9 - Temperature dependence on the (a) bulk and (b) grain boundary conductivities of the different sintering processes, on an Arrhenius plot

III.6 TEM and EDX mapping of the grain boundary

Since the grain boundary conductivity is the limiting factor at low temperature, an in-depth analysis of the specific chemical and morphological features of grain boundaries was performed for each sintering protocol.

The Figure 10a shows a TEM image of the grain boundary of the conventional sintering sample. A specific section of this image was analysed by EDX mapping (mapping of the Yttrium element repartition is shown on Figure 10b) in order to determine the elemental distribution of cations in the grain boundary when using the conventional route. Figure 10c shows the atomic distribution of each element as a function of the position in the area. The HAADF curve corresponds to the intensity of the signal measured at a given pixel. From the HAADF curve, it is possible to see that the grain boundary is located between the 11th and the 20th nm. The mean thickness value of this grain boundary is 8.3 nm. This measurement shows no variation at the grain boundary, meaning that the element repartition is stable. The stoichiometry calculated from the measured elemental concentrations yields a unit formula of

$Ba_{0.85}Zr_{0.75}Ce_{0.24}Y_{0.16}O_{3-\delta}$, which corresponds to a Barium deficiency as compared to the nominal formula of $BaZr_{0.7}Ce_{0.2}Y_{0.1}O_{3-\delta}$.

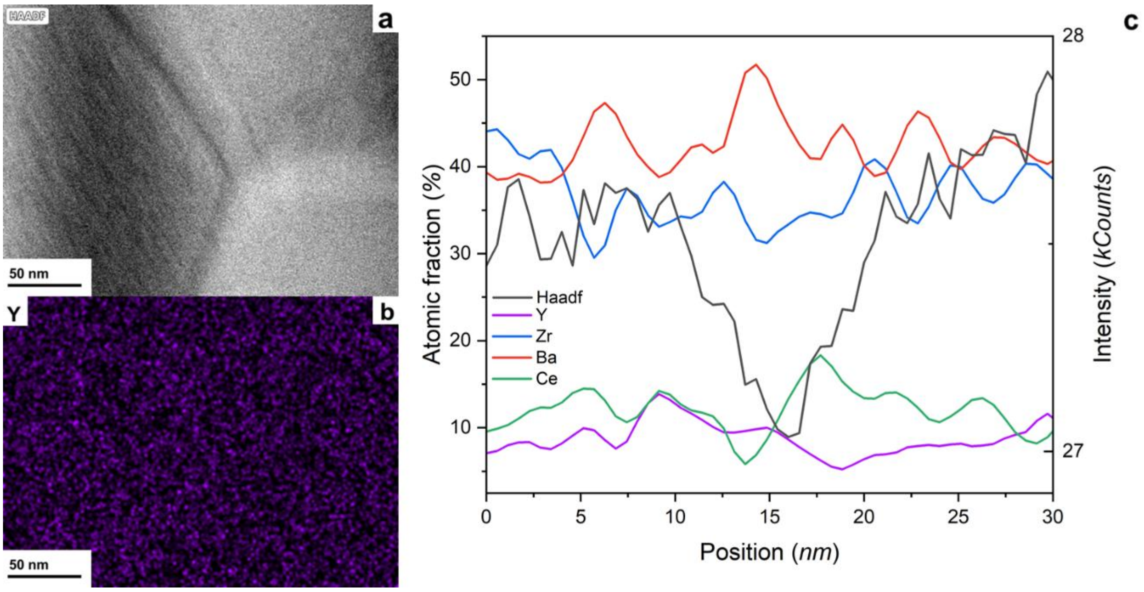

Figure 10 - (a) TEM image of a cross section of $BaZr_{0.7}Ce_{0.2}Y_{0.1}O_{3-\delta}$ electrolyte fabricated using conventional process (b) EDX mapping of the conventional sample grain boundary {Y} and (c) evolution of the atomic distribution as a function of the map position on the sample

The same analysis is performed on a sample fabricated using the CSP sintering strategy. Figure 11 shows TEM images taken on FIB-SEM-thinned lamellae of the electrolyte (Figure11a). A closer image (Figure 11b) reveals the EDX mapping of the grain boundary (yttrium element). Figure 11c shows the atomic distribution of the various elements present at the grain boundary plotted as a function of position on the sample. The grain boundaries of the CSP sample are thinner (7.1 nm) than the conventional one (8.3 nm). Figure 11c shows that, the distribution of the elements is also homogeneous. For the CSP sample, the stoichiometry calculated from the measured elemental concentrations yields a unit formula of $Ba_{0.89}Zr_{0.74}Ce_{0.22}Y_{0.15}O_{3-\delta}$, which also corresponds to a Barium deficiency. This observation suggests that the Barium deficiency originates from the initial composition of the commercial powder, rather that of an effect of the sintering strategies. There is no measurable change of cation concentrations close or in the grain boundary. Previous results showed that grain boundary has a dominant influence on the total conductivity. However, conventional and CSP densification protocols do not seem to influence the grain boundary chemistry.

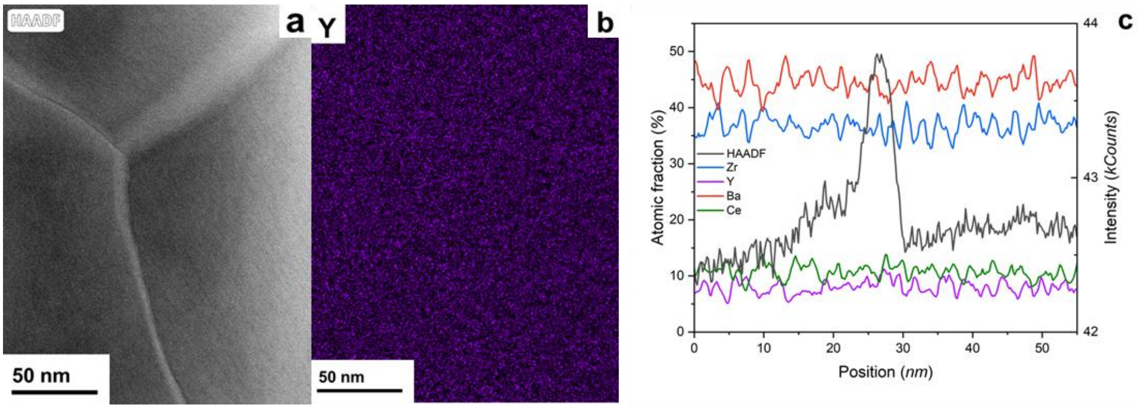

Figure 11 - (a) TEM image of a cross section of $BaZr_{0.7}Ce_{0.2}Y_{0.1}O_{3-\delta}$ electrolyte fabricated using CSP, (b) EDX mapping of the CSP sample grain boundary {Y} and (c) evolution of the atomic distribution as a function of the map position on the sample

Figure 12 shows TEM images of the electrolyte fabricated using ZnO-Li sintering aids. Figure 12a shows the atomic matrix of the grain boundary, the change in structure orientation at the intersection between the two crystals can be observed. Figure 12b and c shows the EDX maps for yttrium and zirconium elements. Finally, Figure 12d shows the atomic distribution of the constituting elements present at the grain boundary, plotted as a function of position on the sample. EDX analysis confirms the presence of the doping element Zn (the technique is not sensitive to lithium). The thickness of the grain boundary reaches 2.9 nm, which is much smaller than for the other routes (7.1 and 8.3 nm). Figure 12b and c shows that, while the distribution of barium, cerium and zinc is homogeneous, an excess of yttrium and a slight deficiency of zirconium is observed at the grain boundary, between 2.5 and 5.5 nm. The Figure 12d, confirms that the distribution of elements inside the bulk structure (from 0 to 2.5 nm and 5.5 to 8.5 nm), corresponds to a $Ba_{0.91}Zr_{0.73}Ce_{0.22}Y_{0.13}O_{3-\delta}$ stoichiometry (the atomic fraction of the elements has been normalized by the presence of zinc) close to the desired one ($BaZr_{0.7}Ce_{0.2}Y_{0.1}O_{3-\delta}$). At the grain boundary, from 2.5 to 5.5 nm, the element distribution corresponds to a stoichiometry with yttrium enrichment: $BaZr_{0.61}Ce_{0.19}Y_{0.2}O_{3-\delta}$.

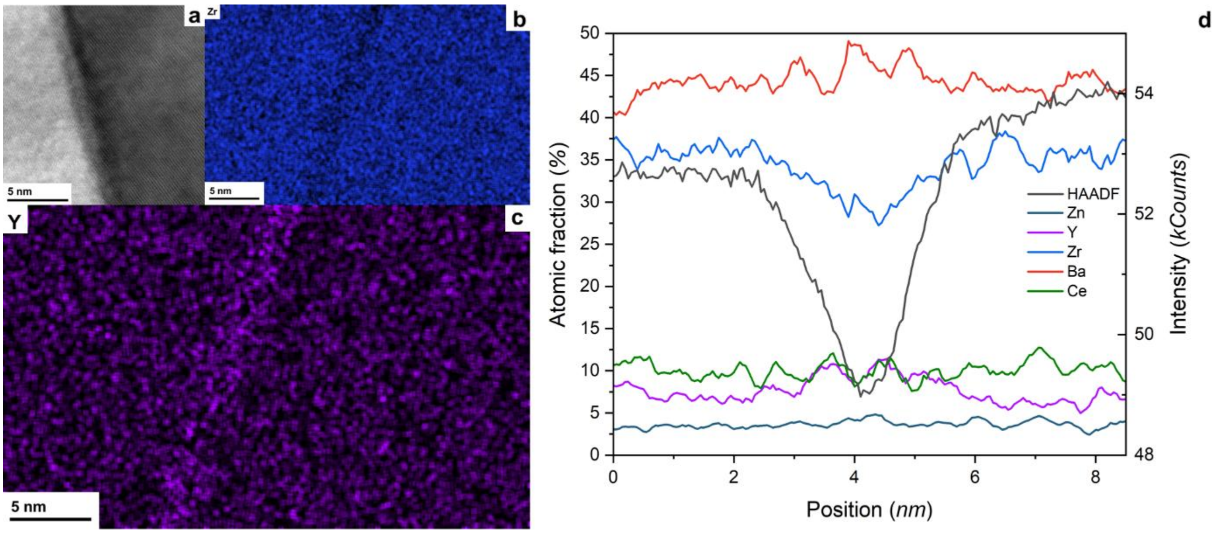

Figure 12 - (a) TEM image of a cross section of $BaZr_{0.7}Ce_{0.2}Y_{0.1}O_{3-\delta}$ *electrolyte fabricated using ZnO-Li, (b and c) EDX mapping of the ZnO-Li sample grain boundary {Zr and Y} and (d) evolution of the atomic distribution as a function of the map position on the sample*

The fine characterization of the grain boundary by TEM and EDX mapping provides information to better explain the discrepancy in grain boundary conductivities revealed by impedance measurements between the different samples. Both Conventional and CSP samples show a similar chemical behaviour at the grain boundary. The elements are well distributed and the stoichiometry of the grain boundary is close to the desired one. In the sample densified with sintering aid, the presence of zirconium deficiencies and high yttrium concentrations influences charge diffusion in this zone. The sintering aids, namely ZnO and Li_2O, because of their low solubility in the perovskite lattice, will segregate at the grain boundary and promote proton diffusion by reducing the space charge barrier. Their presence could also favours the yttrium and zirconium segregation. Higher concentrations in yttrium indicates higher concentrations of oxygen vacancies, thereby increasing the height of the space charge. Therefore, it is easier for the ionic charges to diffuse inside a grain boundary that is parallel to the charge flow. It should also be noted that no excess zinc is observed in the grain boundary zone, which suggests that the beneficial effect of the sintering aid is correlated with densification mechanisms, and not with the change in composition at the grain boundaries. Finally, for every sintering routes, a constant barium deficiency in the structure is observable. During the decomposition of the barium carbonate impurity studied previously, the assumption that the barium was entirely re-dissolved inside the structure was proposed. The TEM analysis shows that this assumption might is not true, and that the initial stoichiometry of the commercial powder used might be deficient in barium.

TEM analysis of the different routes shows variations in morphology (different thicknesses) and chemistry at the grain boundary. To discriminate the two effects, the specific grain boundary conductivity is calculated. The specific grain boundary conductivity Figure 13 has been determined based on the brick layer model [42,43] using equation 4 in the case of $C_{bulk} < C_{gb}$ and where $\sigma_{gb} < \sigma_{bulk}$.

$$\boldsymbol{\sigma_{sp.gb} = \sigma_{gb} * \left(\frac{g}{G}\right)} \tag{4}$$

where, ***g*** is the grain boundary thickness calculated using TEM images and ***G*** the grain thickness given in Table 3. Moreover, σ_{gb} values (displayed in Figure 9b) are obtain by fitting the corresponding Nyquist diagrams and normalized regarding the geometry of the sample. The values of ***g*** and ***G*** used to calculate the specific grain boundary conductivity are detailed in Table 4.

Table 4 – Grain size calculated from SEM images and grain boundary thickness calculated from TEM images

	Conv	CSP	ZnO-Li
G (cm)	$3.5\cdot10^{-5}$	$5.5\cdot10^{-5}$	$3.5\cdot10^{-4}$
g (cm)	$8.3\cdot10^{-7}$	$7.1\cdot10^{-7}$	$2.9\cdot10^{-7}$

Figure 13 shows the temperature dependence of the specific grain boundary conductivities of the different samples, which better represents the grain boundary transport by suppressing volumetric effect. Figure 13 shows that the presence of ZnO-Li has a positive impact on the grain boundary as compared to conventional and CSP sintering, increasing by an order of magnitude the specific conductivity of this sample. On the contrary, the CSP route yields a specific grain boundary conductivity closer to conventional sintering, linked to their similar mean grain boundary thicknesses (respectively 7.1 and 8.3 nm). As already observed by Iguchi *et al.* [44], cation segregations and depletions can readily occurs at the grain boundaries of zirconate ceramics. These imbalances cause a variation of charged defects concentrations in the grain boundary cores, which in turn results in variation of the space charge barriers that protons need to overcome to cross the grain boundary. Then, the wide range between the specific grain boundary conductivity of the ZnO-Li sample and the other strategies could be explained by the observed segregation of Yttrium and depletion of zirconium. Whereas, the specific conductivity similarity between the conventional and CSP routes can be explained by their closed values of grain boundary thickness.

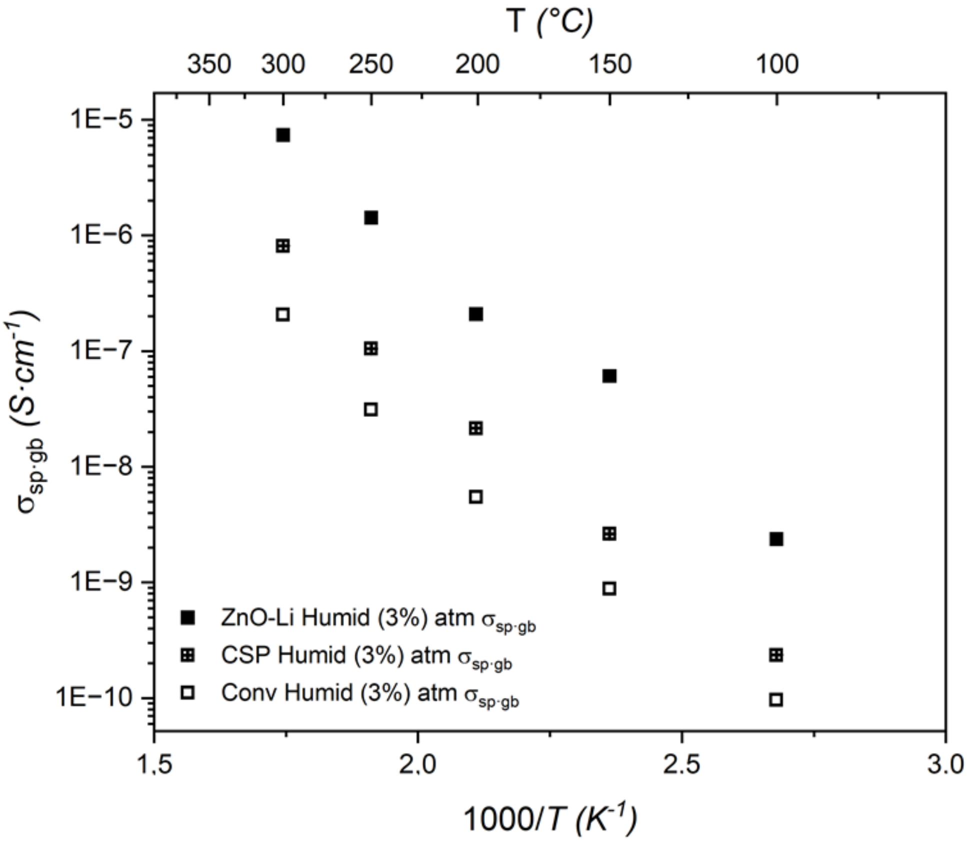

Figure 13 – Conductivity dependence of the specific grain boundary over the temperature range 100 - 350 °C in humid (3 %) atmosphere, of the BZCY-721 electrolytes densified using the different sintering strategies

A first hypothesis would be to imagine that the chemistry of the grain boundary has a dominant influence on its conductivity.

III.7 Total conductivity of the electrolytes

Additionally, the total conductivities are compared over a wider range of temperatures in wet and dry atmospheres (Figure 14 a,b and c). Below 600 °C, in wet air, all the samples show higher conductivity, compared to the dehydrated ones (under dry atm), in accordance with the presence of protons in the lattice. At low temperature, thermal energy is not sufficient for the oxide ion to diffuse easily through the grain boundary due to their high ionic radii. Moreover, the activation energy range from 0.7 to 1 eV of the oxygen-ion diffusion requires higher temperatures (From 600 °C to 1100 °C) to increase the charge mobility in the electrolyte structure [45–47]. For protonic species, smaller than the oxide ions, the activation energy for diffusion is lower (0.4-0.55 eV), thus increasing the conductivity at lower temperatures. At temperatures above 600 °C, proton concentration decreases as a result of dehydration [48], which reduces the protonic conductivity accordingly. Therefore, the conductivity is primarily that of the oxygen-ion vacancies, which is consistent with the observed change of activation from 0.5 eV to 0.7-0.8 eV and an overlap between the conductivities in wet and dry atmospheres. For the sample with sintering aid (Figure 14c), the overlap between protonic and oxygen-ion conduction occurs at a temperature below 600 °C. This behaviour suggest that the chemistry of the grain boundary has also an influence on the dehydration processes.

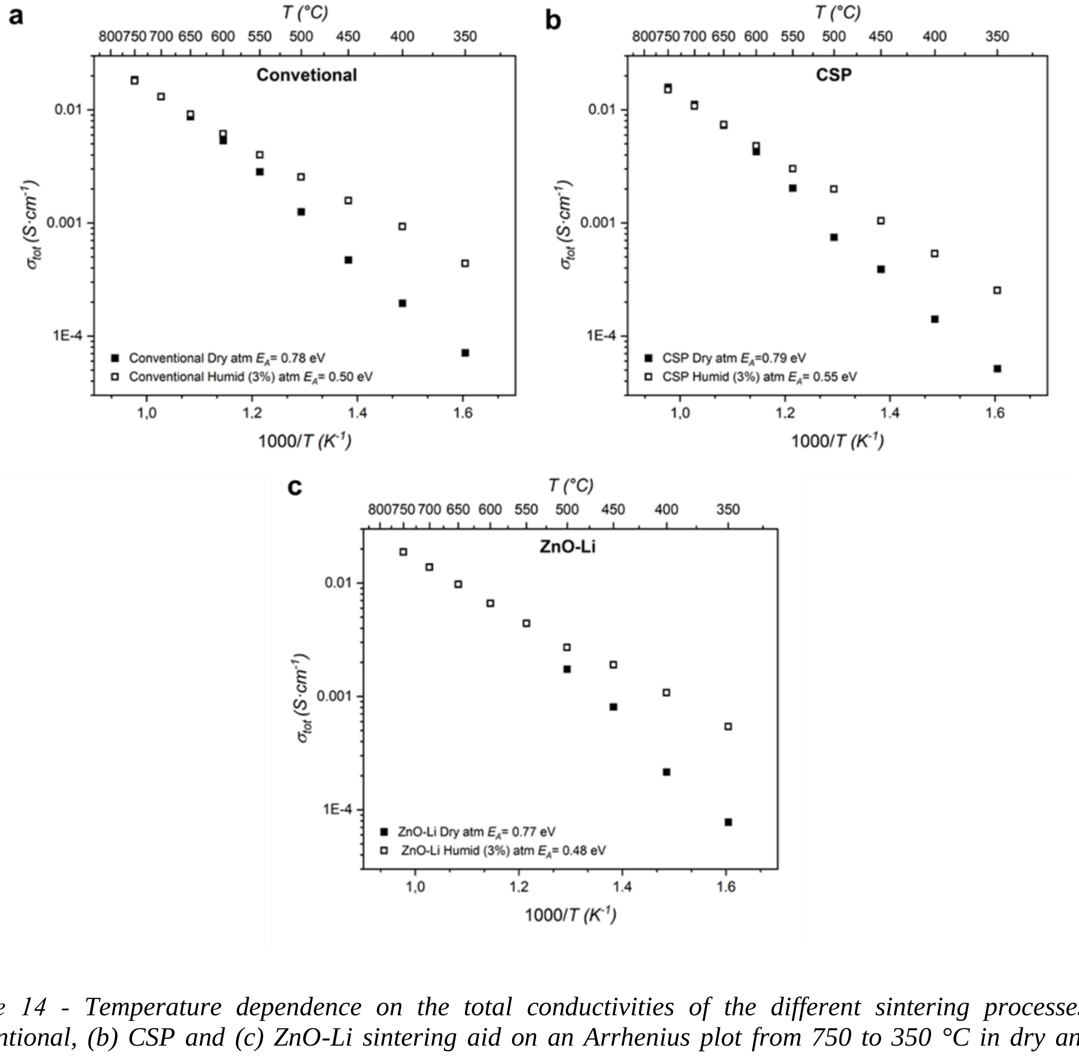

Figure 14 - Temperature dependence on the total conductivities of the different sintering processes; (a) conventional, (b) CSP and (c) ZnO-Li sintering aid on an Arrhenius plot from 750 to 350 °C in dry and wet atmospheres

Table 5 compares the values of total conductivities of the different samples. The conventionally sintered electrolyte yields a conductivity of $1.6\cdot10^{-3}$ $S\cdot cm^{-1}$ at 450 °C in wet air and $4.7 \cdot 10^{-4}$ S·cm^{-1} in dry air. Therefore, the specific protonic conductivity extracted by subtracting the dry conductivity to the total one, yields $1.13 \cdot 10^{-3}$ S·cm^{-1}. At 450 °C the best conductivity is observed with the ZnO-Li sample in wet air ($2 \cdot 10^{-3}$ S·cm^{-1}), increasing by one order of magnitude the conductivity compared to the dry atmosphere. At 750 °C, where the conductivity is dominated by oxygen-ion transport, the electrolyte samples yield comparable total conductivities, between 1.5 and $2 \cdot 10^{-2}$ S·cm^{-1}.

Table 5. *Relative density values calculated from the lattice volume and geometrical parameters of the different samples. Activation energies of the total conductivities under dry and humid (3 %) atmospheres, and total conductivities of the samples at 450 °C and 750 °C.*

	Relative density (%)	E_A wet atm (eV)	E_A dry atm (eV)	σ_{tot} 450 °C wet (S·cm^{-1})	σ_{tot} 450 °C dry (S·cm^{-1})	σ_{tot} 750 °C (S·cm^{-1})
Conv	90	0.50	0.78	$1.6 \cdot 10^{-3}$	$4.7 \cdot 10^{-4}$	$1.8 \cdot 10^{-2}$
CSP	91	0.55	0.79	$1 \cdot 10^{-3}$	$3.9 \cdot 10^{-4}$	$1.6 \cdot 10^{-2}$
ZnO-Li	95	0.48	0.77	$2 \cdot 10^{-3}$	$8 \cdot 10^{-4}$	$1.9 \cdot 10^{-2}$

III.8 Towards decreasing the sintering temperature

One of the motivations for this study was to better understand the densification behaviour of the $BaZr_xCe_{0.9-x}Y_{0.1}O_{3-\delta}$ electrolyte material in order to reduce its sintering temperature. Figure 15 shows the total conductivity of a sample, fabricated using the CSP protocol, densified at 1500 °C for 15 h, compared to the former CSP sample densified at 1600 °C for 15 h. At 500 °C, it is possible to observe constant conductivity for both samples around $2 \cdot 10^{-3}$ S·cm^{-1}. The conductivity remains constant even though the relative density of the sample respectively going from 91 to 88 %. CSP samples have also been fabricated using lower temperature (1400 – 1300 – 1200 °C), however, at this temperature the densification process is not sufficient and the pellets are too brittle to be measurable.

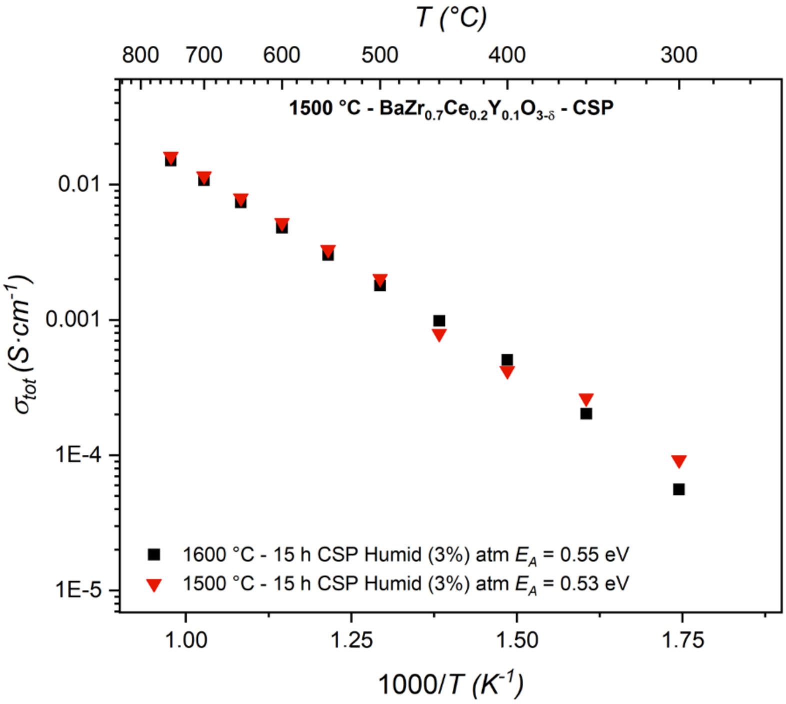

Figure 15 - Total conductivities of densified $BaZr_{0.7}Ce_{0.2}Y_{0.1}O_{3-\delta}$ *electrolyte using CSP, at decreasing temperatures, 1600 °C for 15 h and 1500 °C for 15 h*

In view of the promising results obtained with the ZnO-Li aid, several $BaZr_{0.7}Ce_{0.2}Y_{0.1}O_{3-\delta}$ samples were densified with this aid at lower temperatures (1500 - 1400 - 1300 °C) while maintaining this temperature the longer the lower the temperature (15 - 20 - 25 h respectively). Figure 16 shows SEM images of cross-sections of the various samples. These images show that the structure is homogeneous and completely dense (around 93 % relative density). It is therefore possible to achieve complete densification of the $BaZr_{0.7}Ce_{0.2}Y_{0.1}O_{3-\delta}$ material using a suitable heat treatment (1300 °C for 25 h) and the sintering aid of ZnO-Li.

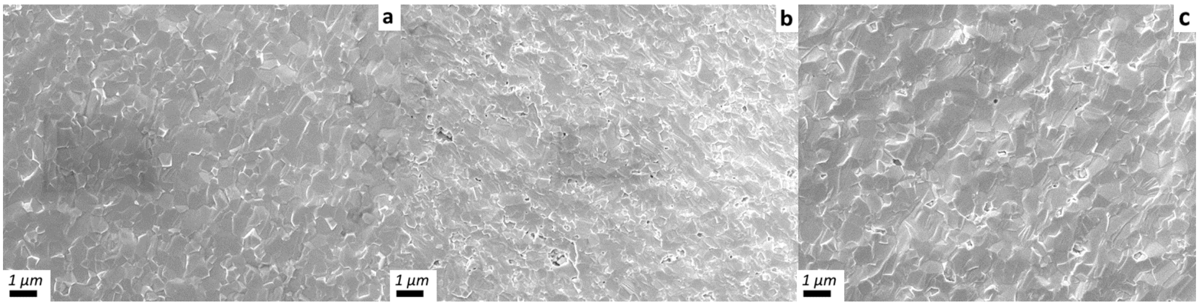

Figure 16 – SEM images of a cross section of the ZnO-Li sample sintered at (a) 1500 °C for 15 h, (b) 1400 °C for 20 h and (c) 1300 °C for 25 h

Figure 17 shows the evolution of the total conductivity of the electrolyte under humid air (3 %) as a function of the densification temperature, compared with that of the initial sample densified at 1600 °C for 15 h. At 500 °C, all samples show a total conductivity of $3 \cdot 10^{-3}$ $S \cdot cm^{-}$

[1]. It is therefore possible to lower the sintering temperature by around 300 °C using the ZnO-Li sintering aid and a longer densification step (25 h), without impacting the performance of the electrolyte material.

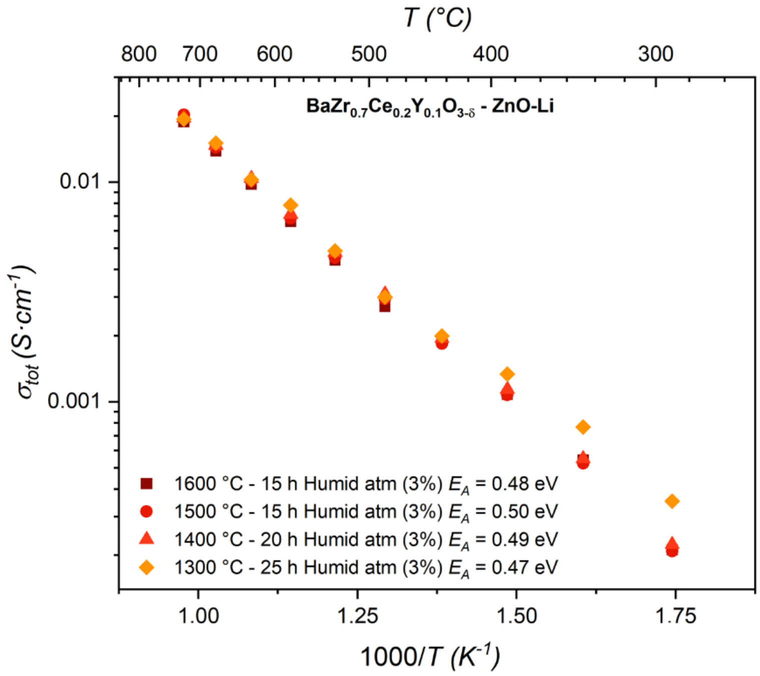

Figure 17 – Total conductivities of densified BaZr$_{0.7}$Ce$_{0.2}$Y$_{0.1}$O$_{3-\delta}$ electrolyte using the ZnO-Li sintering aid, at decreasing temperatures, 1600 °C for 15 h, 1500 °C for 15 h, 1400 °C for 20 h and 1300 °C for 25 h

IV. Conclusion

The densification mechanisms of zirconium-rich BaZr$_{0.7}$Ce$_{0.2}$Y$_{0.1}$O$_{3-\delta}$ electrolytes based on commercial powders using different protocols have been studied. XRD diagrams of the powder material showed the presence of a barium carbonate impurity, which completely decomposes at 1100 °C, leaving a pure crystalline phase of the electrolyte material after a high temperature treatment (1600 °C). From this powder, electrolyte pellets have been synthetized using conventional pressing, CSP, or 1 wt.% of ZnO-Li sintering aid. The three samples were post-sintered at 1600 °C for 15 h. The densification process was characterized by dilatometry. A volume increase, associated to the decomposition of the barium carbonate is observed between 1100 °C and 1450 °C. TGA and DSC results confirm that the disruption is due to the decomposition of the barium carbonate impurity and the dissolution of the barium back in the perovskite lattice. The characterization of the morphology shows that improved densification method such as CSP or the addition of sintering aids have a direct impact on the grain growth, thus giving higher relative density. The conductivity of the samples has been characterized using EIS. At temperatures below 350 °C, the grain boundary is the limiting factor to the conductivity of the electrolyte. Concerning CSP and conventional strategies, the specific grain boundary conductivity showed similar results. However, the ZnO-Li sample showed an improved specific grain boundary conductivity. The TEM analysis conducted shows that, even if it favours a higher conductivity of the material through a better densification (grain boundary thickness equals 2.9 nm), using sintering aids such as ZnO-Li influences the chemistry of the grain boundary. Higher concentrations of yttrium and a zirconium deficiency can be observed at the grain boundary. Moreover, the TEM analysis of the conventional and CSP sample shows a thicker grain boundary (respectively 8.3 and 7.1 nm). However, the latter demonstrates a homogeneous repartition of the elements at the grain boundary. Finally, for each sample, a general barium deficiency is observed.

At temperature between 350 and 600 °C under humid atmosphere, the study showed that the protonic behaviour of the material increases by one order of magnitude the total conductivity. The sintered aided electrolyte (95 % relative density) yields a conductivity of $2{\cdot}10^{-3}$ $S{\cdot}cm^{-1}$ at 450 °C in wet air and $8{\cdot}10^{-4}$ $S{\cdot}cm^{-1}$ in dry air. The specific protonic conductivity is then extracted yielding $1.2{\cdot}10^{-3}$ $S{\cdot}cm^{-1}$. Finally, at high temperature (750 °C), conductivity is dominated by oxide ion diffusion, and all electrolyte samples yields total conductivities of $2{\cdot}10^{-2}$ $S{\cdot}cm^{-1}$, regardless of the processing route.

Finally, while using the sintering aid strategy, sintering temperature of the sample has been decreased from 1600 °C during 15 h to 1300 °C during 25 h. While using this new protocol, the sample showed equivalent relative density (93 %) and total conductivity ($3{\cdot}10^{-3}$ $S{\cdot}cm^{-1}$ at 500 °C)

V. Acknowledgments

This work is part of ARCADE Franco German ANR/BMBF project (ANR-19-ENR-0003) "Advanced and Robust metal supported Cell with proton conducting ceramic for electrolysis Applications in defossilized Energy systems". Funding by the French Contrat Plan État-Région and the European Regional Development Fund of Pays de la Loire and the CIMEN Electron Microscopy Center in Nantes, are greatly acknowledged.

VI. References

[1] Turner JA. Sustainable Hydrogen Production. Science 2004;305:972–4. https://doi.org/10.1126/science.1103197.

[2] Hanif MB, Rauf S, Motola M, Babar ZUD, Li C-J, Li C-X. Recent progress of perovskite-based electrolyte materials for solid oxide fuel cells and performance optimizing strategies for energy storage applications. Materials Research Bulletin 2022;146:111612. https://doi.org/10.1016/j.materresbull.2021.111612.

[3] Bi L. Steam electrolysis by solid oxide electrolysis cells (SOECs) with proton-conducting oxides. Chem Soc Rev 2014:16.

[4] Fan L, Zhu B, Su P-C, He C. Nanomaterials and technologies for low temperature solid oxide fuel cells: Recent advances, challenges and opportunities. Nano Energy 2018;45:148–76. https://doi.org/10.1016/j.nanoen.2017.12.044.

[5] Iwahara H, Esaka T, Uchida H, Maeda N. Proton conduction in sintered oxides and its application to steam electrolysis for hydrogen production. Solid State Ionics 1981;3–4:359–63. https://doi.org/10.1016/0167-2738(81)90113-2.

[6] Iwahara H. Proton conducting ceramics and their applications. Solid State Ionics 1996;86–88:9–15. https://doi.org/10.1016/0167-2738(96)00087-2.

[7] Ryu KH, Haile SM. Chemical stability and proton conductivity of doped BaCeO3–BaZrO3 solid solutions. Solid State Ionics 1999;125:355–67. https://doi.org/10.1016/S0167-2738(99)00196-4.

[8] Wendler LP, Ramos K, Souza DMPF. Investigation about the reason of limited grain growth of Y-doped barium zirconate. Ceramics International 2019;45:19120–6. https://doi.org/10.1016/j.ceramint.2019.06.158.

[9] Babilo P, Haile SM. Enhanced Sintering of Yttrium-Doped Barium Zirconate by Addition of ZnO. J American Ceramic Society 2005;88:2362–8. https://doi.org/10.1111/j.1551-2916.2005.00449.x.

[10] Kim H-W, Seo J, Yu JH, Yun KS, Joo JH, Moon J, et al. Effect of cerium on yttrium-doped barium zirconate with a ZnO sintering aid: Grain and grain boundary protonic conduction. Ceramics International 2021;47:32720–6. https://doi.org/10.1016/j.ceramint.2021.08.168.

[11] Gao D, Guo R. Structural and electrochemical properties of yttrium-doped barium zirconate by addition of CuO. Journal of Alloys and Compounds 2010;493:288–93. https://doi.org/10.1016/j.jallcom.2009.12.082.

[12] Ricote S, Bonanos N, Manerbino A, Coors WG. Conductivity study of dense BaCexZr(0.9−x)Y0.1O(3−δ) prepared by solid state reactive sintering at 1500 °C. International Journal of Hydrogen Energy 2012;37:7954–61. https://doi.org/10.1016/j.ijhydene.2011.08.118.

[13] Nasani N, Dias PAN, Saraiva JA, Fagg DP. Synthesis and conductivity of Ba(Ce,Zr,Y)O3−δ electrolytes for PCFCs by new nitrate-free combustion method. International Journal of Hydrogen Energy 2013;38:8461–70. https://doi.org/10.1016/j.ijhydene.2013.04.078.

[14] Handwerker CA, Blendell JE, Coble RL. SINTERING OF CERAMICS n.d.

[15] Kim H-W, Seo J, Yu JH, Yun KS, Joo JH, Moon J, et al. Effect of cerium on yttrium-doped barium zirconate with a ZnO sintering aid: Grain and grain boundary protonic conduction. Ceramics International 2021;47:32720–6. https://doi.org/10.1016/j.ceramint.2021.08.168.

[16] Hostaša J, Picelli F, Hříbalová S, Nečina V. Sintering aids, their role and behaviour in the production of transparent ceramics. Open Ceramics 2021;7:100137. https://doi.org/10.1016/j.oceram.2021.100137.

[17] Li Y, Guo R, Wang C, Liu Y, Shao Z, An J, et al. Stable and easily sintered BaCe0.5Zr0.3Y0.2O3−δ electrolytes using ZnO and Na2CO3 additives for protonic oxide fuel cells. Electrochimica Acta 2013;95:95–101. https://doi.org/10.1016/j.electacta.2013.02.023.

[18] Babar ZUD, Hanif MB, Gao J-T, Li C-J, Li C-X. Sintering behavior of BaCe0.7Zr0.1Y0.2O3-δ electrolyte at 1150 °C with the utilization of CuO and Bi2O3 as sintering aids and its electrical performance. International Journal of Hydrogen Energy 2022;47:7403–14. https://doi.org/10.1016/j.ijhydene.2021.12.075.

[19] Yuehua Li, Wenjie Yang, Ling Wang, Jing Zhu, Wei Meng, Zhangxing He, Lei Dai. Improvement of sinterability of BaZr0.8Y0.2O3-δ for H2 separation using Li2O/ZnO dual-sintering aid 2018:15935–43.

[20] Guo J, Floyd R, Lowum S, Maria J-P, Herisson de Beauvoir T, Seo J-H, et al. Cold Sintering: Progress, Challenges, and Future Opportunities. Annu Rev Mater Res 2019;49:275–95. https://doi.org/10.1146/annurev-matsci-070218-010041.

[21] Thabet K, Quarez E, Joubert O, Le Gal La Salle A. Application of the cold sintering process to the electrolyte material BaCe0.8Zr0.1Y0.1O3-δ. Journal of the European Ceramic Society 2020;40:3445–52. https://doi.org/10.1016/j.jeurceramsoc.2020.03.043.

[22] Petříček V, Dušek M, Palatinus L. Crystallographic Computing System JANA2006: General features. Zeitschrift Für Kristallographie - Crystalline Materials 2014;229:345–52. https://doi.org/10.1515/zkri-2014-1737.

[23] Cheary RW, Coelho AA. Axial Divergence in a Conventional X-ray Powder Diffractometer. I. Theoretical Foundations. J Appl Crystallogr 1998;31:851–61. https://doi.org/10.1107/S0021889898006876.

[24] Bérar JF, Lelann P. E.s.d.'s and estimated probable error obtained in Rietveld refinements with local correlations. J Appl Crystallogr 1991;24:1–5. https://doi.org/10.1107/S0021889890008391.

[25] Khan K, Babar Z uD D, Qayyum S, Hanif MB, Rauf S, Sultan A, et al. Design of efficient and durable symmetrical protonic ceramic fuel cells at intermediate temperatures via B-site doping of Ni in BaCe0.56Zr0.2Ni0.04Y0.2O3–δ. Ceramics International 2023;49:16826–35. https://doi.org/10.1016/j.ceramint.2023.02.043.

[26] Bondevik T, Polfus JM, Norby T. Disagreements between space charge models and grain boundary impedance data in yttrium-substituted barium zirconate. Solid State Ionics 2020;353:115369. https://doi.org/10.1016/j.ssi.2020.115369.

[27] Mather GC, Heras-Juaristi G, Ritter C, Fuentes RO, Chinelatto AL, Pérez-Coll D, et al. Phase Transitions, Chemical Expansion, and Deuteron Sites in the $BaZr_{0.7}Ce_{0.2}Y_{0.1}O_{3-\delta}$ Proton Conductor. Chem Mater 2016;28:4292–9. https://doi.org/10.1021/acs.chemmater.6b01095.

[28] J. Wallis, L. Urban. Structural and electrical properties of BaZr0.7Ce0.2Y0.1O3−δ proton conducting ceramic fabricated by spark plasma sintering 2019.

[29] Pandey BK, Shahi AK, Shah J, Kotnala RK, Gopal R. Giant ferromagnetism in Li doped ZnO nanoparticles at room temperature. Journal of Alloys and Compounds 2020;823:153710. https://doi.org/10.1016/j.jallcom.2020.153710.

[30] Shawuti S, Sherwani A ur R, Can MM, Gülgün MA. Complex Impedance Analyses of Li doped ZnO Electrolyte Materials. Sci Rep 2020;10:8228. https://doi.org/10.1038/s41598-020-65075-0.

[31] Haile SM, West DL, Campbell J. The role of microstructure and processing on the proton conducting properties of gadolinium-doped barium cerate. J Mater Res 1998;13:1576–95. https://doi.org/10.1557/JMR.1998.0219.

[32] Bach M, Schemmel T, Hubálková J, Bühringer M, Jansen H, Aneziris CG. Effect of thermal treatment conditions on the solid-state synthesis of barium zirconate from barium carbonate and monoclinic zirconia. Ceramics International 2021;47:25839–45. https://doi.org/10.1016/j.ceramint.2021.05.313.

[33] Zhu Z, Hou J, He W, Liu W. High-performance Ba(Zr 0.1 Ce 0.7 Y 0.2)O 3−δ asymmetrical ceramic membrane with external short circuit for hydrogen separation. Journal of Alloys and Compounds 2016;660:231–4. https://doi.org/10.1016/j.jallcom.2015.11.065.

[34] Peng J, Li H, Yan D. Fabrication of yttrium-doped barium zirconate ceramic by high pressure sintering. Ceramics International 2019;45:9310–2. https://doi.org/10.1016/j.ceramint.2019.01.229.

[35] Babilo P, Haile SM. Enhanced Sintering of Yttrium-Doped Barium Zirconate by Addition of ZnO. J American Ceramic Society 2005;88:2362–8. https://doi.org/10.1111/j.1551-2916.2005.00449.x.

[36] Miller MF, Woodward JR, Bailey E, Thiemens MH, McMillan PF, Grady MM, et al. Mass-independent fractionation of oxygen isotopes during thermal decomposition of divalent metal carbonates: Crystallographic influence, potential mechanism and cosmochemical significance. Chemical Geology 2021;586:120500. https://doi.org/10.1016/j.chemgeo.2021.120500.

[37] Qiao Z, Li S, Li Y, Wang J. Properties of barium zirconate sintered from different barium and zirconium sources. Ceramics International 2021;47:31194–201. https://doi.org/10.1016/j.ceramint.2021.07.295.

[38] Liu W, Chu G-W, Li S-C, Bai S, Luo Y, Sun B-C, et al. Preparation of lithium carbonate by thermal decomposition in a rotating packed bed reactor. Chemical Engineering Journal 2019;377:119929. https://doi.org/10.1016/j.cej.2018.09.090.

[39] Arvanitidis I, Sichen D, Seetharaman S. A Study of the Thermal Decomposition of BaC03. METALLURGICAL AND MATERIALS TRANSACTIONS B n.d.

[40] Huang Q-A, Hui R, Wang B, Zhang J. A review of AC impedance modeling and validation in SOFC diagnosis. Electrochimica Acta 2007;52:8144–64. https://doi.org/10.1016/j.electacta.2007.05.071.

[41] Merkle R, Hoedl MF, Raimondi G, Zohourian R, Maier J. Oxides with Mixed Protonic and Electronic Conductivity. Annu Rev Mater Res 2021;51:461–93. https://doi.org/10.1146/annurev-matsci-091819-010219.

[42] Haile SM, West DL, Campbell J. The role of microstructure and processing on the proton conducting properties of gadolinium-doped barium cerate. J Mater Res 1998;13:1576–95. https://doi.org/10.1557/JMR.1998.0219.

[43] Peters C, Weber A, Butz B, Gerthsen D, Ivers-Tiffée E. Grain-Size Effects in YSZ Thin-Film Electrolytes. Journal of the American Ceramic Society 2009;92:2017–24. https://doi.org/10.1111/j.1551-2916.2009.03157.x.

[44] Iguchi F, Tsurui T, Sata N, Nagao Y, Yugami H. The relationship between chemical composition distributions and specific grain boundary conductivity in Y-doped BaZrO3 proton conductors. Solid State Ionics 2009;180:563–8. https://doi.org/10.1016/j.ssi.2008.12.006.

[45] INITIAL STAGE SINTERING n.d.

[46] Wang H, Peng R, Wu X, Hu J, Xia C. Sintering Behavior and Conductivity Study of Yttrium-Doped BaCeO $_3$ -BaZrO $_3$ Solid Solutions Using ZnO Additives. Journal of the

American Ceramic Society 2009;92:2623–9. https://doi.org/10.1111/j.1551-2916.2009.03204.x.

[47] Wallis J., Ricote S. The influence of the sintering temperature on BaZr0·7Ce0·2Y0·1O3-δ proton conductors prepared by Spark Plasma Sintering 2021.

[48] Quarez E, Noirault S, Caldes MT, Joubert O. Water incorporation and proton conductivity in titanium substituted barium indate. Journal of Power Sources 2010;195:1136–41. https://doi.org/10.1016/j.jpowsour.2009.08.086.